Materials Advances

ROYAL SOCIETY OF CHEMISTRY

PAPER

View Article Online
View Journal | View Issue

Cite this: *Mater. Adv.*, 2021, 2, 3346

Eu^{3+}-functionalized CQD hybrid material: synthesis, luminescence properties and sensing application for the detection of Cu^{2+}†

Ying Li,[a] Dan Liu,[a] Ya-Qi Wang,[a] Fang-Fang Wang[b] and Han-Xun Qiu*[a]

Received 24th January 2021,
Accepted 22nd March 2021

DOI: 10.1039/d1ma00059d

rsc.li/materials-advances

In this study, we developed a novel flexible method to construct a lanthanide dual-emitting ratiometric fluorescence nanoprobe with excellent luminescence properties and significant selectivity for the detection of copper ions, where the central Eu^{3+} ions are coordinated with 2,6-pyridinedicarboxylic acid (DPA) on the surface of CQDs. The structure and chemical sensing photoluminescence properties of the as-prepared fluorescent probe have been investigated in detail. Moreover, the results have shown that Eu-DPA–CQDs exhibit two fluorescence emissions at 450 nm and 613 nm, respectively, under an excitation wavelength of 285 nm. The responses of the two emissions towards Cu^{2+} ions are completely different and can provide references for each other. Therefore, it can be designed as a fluorescence sensor for the detection of Cu^{2+} ions. The emission spectrum at 613 nm is markedly quenched, while that at 450 nm slightly changed after the addition of Cu^{2+} ions. When the Cu^{2+} ion concentration was 0–150 μM, the FL ratio (I_{Eu}/I_{CQDs}) showed a good linear relationship with the lowest detection limit (LOD) of 6 nM. Thus, the reported sensor has a high selectivity, satisfactory accuracy and precision, and it may provide the potential application in the biological and environmental fields.

1. Introduction

With the recent industrial development, excess metal ions in water may cause considerable harm to the human body, and trace amounts of Cu^{2+} ions have been widely detected in recent years. Copper is one of the essential elements for the survival of humans and any other organic organisms because it plays an indispensable role in numerous physiological processes and biochemical systems and has effects on human hematopoiesis, cell growth, and endocrine function.[1,2] Excess Cu^{2+} may cause numerous diseases in human body, including abdominal pain, colic, nausea and vomiting.[3,4] Copper ions in the human body are also mainly used as catalytic cofactors or structural components of numerous enzymes and proteins to participate in cell metabolism. If the Cu^{2+} content in domestic water exceeds that of the standard, it will not only damage crops and other organisms, but also cause irreversible damage to the human body, such as human heart, liver and kidneys.[5] Therefore, the quantification and detection of copper ions is critical.

Recently, the fluorescence detection technology has attracted increasing attention in the detection of numerous metal ions. Carbon quantum dots (CQDs) have a wide application in fluorescence detection, which is attributed to their unique properties. Carbon dots have been used in various aspects, including cell imaging,[6] fluorescent ink,[7] photocatalysis,[8,9] drug delivery,[10] ion detection,[11–17] energy storage[18] and optoelectronics.[19] However, the lower fluorescence quantum yields and the singleness of CQD sensors have limited their practical applications. Furthermore, a single CQD-based sensor is also usually subject to strong interference from the matrix material.[20,21] Lanthanide complexes have a long-life emission and other excellent characteristics, including tunable emission bands and high color purity.[22–24] The ratiometric fluorescence sensor can be used as an ideal substitute by a single excitation. A single emission fluorescence sensor is easily impacted by the instrument's performance, test environment, complex matrix, photobleaching and other factors. In such circumstances, a dual emission fluorescence sensor can solve the inherent weakness of the above single emission. Therefore, the combination of CQDs and lanthanide complexes can obtain excellent composite materials, whose performance is significantly better than that of a single component.

Herein, we developed a novel portable detector for the Cu^{2+} ion detection analysis in daily life. The luminescence center of the detector was the as-prepared Eu-DPA–CQD, which was

[a] School of Materials Science & Engineering, University of Shanghai for Science and Technology, Shanghai 200093, P. R. China. E-mail: hxqiu@usst.edu.cn
[b] The National Facility for Protein Science in Shanghai (NFPS), Shanghai 201210, P. R. China

† Electronic supplementary information (ESI) available. See DOI: 10.1039/d1ma00059d

synthesized by a hydrothermal and ion replacement method. For Mn^{2+}, Zn^{2+}, Ni^{2+}, Cd^{2+}, Fe^{2+}, Co^{2+}, and Fe^{3+} ions, Cu^{2+} ions showed an excellent Cu^{2+} ratio luminescence response. In this system, the two light-emitting centers were the fluorescence of Eu^{3+} ions (λ = 613 nm) and the CQDs (λ = 450 nm), which made the sensing results more reliable. Eu^{3+} has the unique characteristics of Ln^{3+} ions. 2,6-Pyridinedicarboxylic acid (DPA) can provide both the oxygen atom and the nitrogen atom to coordinate with the central Eu^{3+} ions to form a bright red fluorescence emission *via* an energy transfer. As a result, the ratiometric fluorescence sensor can be used as a response signal to exhibit the high selectivity towards Cu^{2+} ions.

2. Experimental section

2.1 Chemicals and materials

Citric acid, sodium hydroxide, nickel chloride, zinc chloride, sodium chloride, diaminonaphthalene, and ammonia water were purchased from the Sinopharm Group Chemical Reagent Co., Ltd (Shanghai, China). Manganese chloride, copper chloride, ferric chloride, ferrous chloride, chromium trichloride, sulfuric acid and 2,6-pyridinedicarboxylic acid (DPA) were purchased from Aladdin (Shanghai, China) and used as received without further purification.

2.2 Instruments

Fourier-transform infrared (FT-IR) spectra were recorded at an infrared spectrophotometer range of 4000 to 400 cm^{-1} by the KBr pellet pressing method. X-ray photoelectron spectroscopy (XPS) patterns were collected on a Thermo ESCALAB 250XI (Science Compass). The UV-Vis absorption spectra were recorded on a UV-Vis spectrometer (Lambda FEG 450, US PEI Co., Ltd). Fluorescence spectra were collected on a quartz cell with an optical path of 200–770 nm at room temperature using an RF-5301 (PC) S 220 V fluorescent spectrophotometer from Shimadzu Corporation, Japan.

2.3 Synthesis of CQDs and the Eu^{3+} complex-functionalized CQDs (defined as Eu-DPA–CQDs)

CQDs were synthesized *via* a typical solvothermal treatment procedure using citric acid and diaminonaphthalene. About 100 mg citric acid and 20 mg diaminonaphthalene were added to 15 ml ethanol to form a transparent solution. Then, the transparent precursor solution was transferred to an 25 ml polytetrafluoroethylene autoclave and heated at 160 °C for 6 h. About 20 ml water was added to dissolve the formed CQDs at room temperature. In order to perform surface amination, about 3 ml ammonium hydroxide was added to the obtained CQD solution, and then the solvothermal synthesis was performed at 200 °C for 1 h. Finally, dry CQDs were obtained *via* the lyophilization of the remaining water solution.

Eu-DPA–CQDs were synthesized as follows: DPA (2 mmol) and $EuCl_3{\cdot}6H_2O$ (2 mmol) were mixed in a 20 ml ethanol solution to form a Eu-DPA solution. Then, a small amount of CQDs was added and refluxed at 80 °C for 5 h. The solution was dialyzed in a membrane tube of 3500 molecular weight ethanol solution for 48 h and was collected for the next experiment (Scheme 1).

2.4 Fluorescence detection process of metal Cu^{2+}

The luminescence properties of pure CQDs and Eu-DPA–CQDs were studied in the Eu-DPA–CQD liquid state at room temperature. The Eu-DPA–CQDs (3 mg) were dissolved in numerous cationic aqueous solutions (Fe^{3+}, Fe^{2+}, Cu^{2+}, Mn^{2+}, Co^{2+}, Zn^{2+}, Ni^{2+}, and Cd^{2+}) to identify the sensitivity and selectivity of this sensor. Then, the solution was dispersed for about 30 min and placed in a fluorescence spectrophotometer to detect the relative fluorescence intensity. Finally, under optimal conditions, the as-prepared Eu-DPA–CQDs were added to the standard solution of Cu^{2+} ions

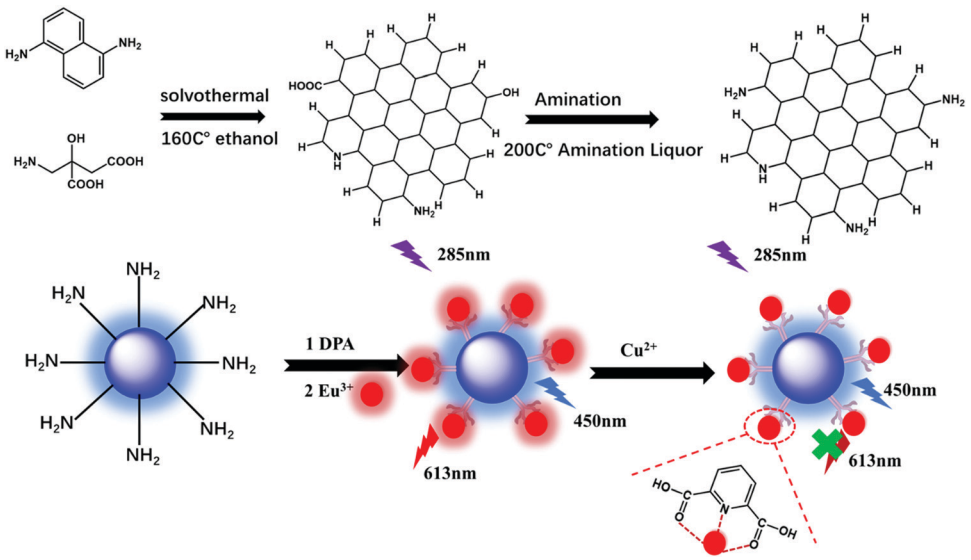

Scheme 1 The synthetic scheme of the Eu-DPA–CQD sensor for the detection of Cu^{2+}.

with different gradient concentrations, and the mixture was subjected to FL measurements. All of the measurements were repeated three times.

2.5 Photoluminescence stability experiment

Initially, 3 mg of the Eu-DPA–CQD powder was simply immersed into different pH solutions. The sample was dispersed ultrasonically for 30 min, and then, the fluorescence analysis was performed at an excitation wavelength of 320 nm. As shown in Fig. S1A (ESI†), in order to ensure the intensity and stability of the double-peak emission of the fluorescent composite, we explored the Eu-DPA–CQD powder dissolved in different amounts of deionized water (5 ml, 10 ml, 15 ml, 20 ml, and 25 ml). It can be observed that the FL emission peak intensity of Eu^{3+} gradually increased with an increase in the dilution factor, until it reached the strongest peak when it was dissolved in 20 ml deionized and tended to be stable. Furthermore, the FL intensity showed a downward trend. Therefore, subsequent experiments uniformly chose the sample concentration as 3 mg/20 ml. Moreover, it can be clearly seen that the ratio of I_{Eu}/I_{CQDs} in the range of 0–30 s dropped sharply, indicating that an immediate response of the fluorescent probe and the emission peak of Eu^{3+} quenched, the response speed was rapid, and the probe gradually demonstrated a stable trend within 120–360 s, and there is basically no difference in the fluorescence ratio at 120 s (Fig. S1B, ESI†). Therefore, the optimal incubation time was set to be at 120 s.

3. Results and discussion

3.1 Structural characterization of Eu-DPA–CQDs

The structure and morphology of the CQDs and Eu-DPA–CQDs were confirmed by FT-IR, TEM, and XPS analyses. The FT-IR spectra were obtained to characterize Eu-DPA–CQDs. Compared to the FT-IR spectra of Eu-DPA (Fig. 1) and DPA (Fig. S2, ESI†), it can be clearly seen that the peak vibration of C═O stretched from 1363 cm^{-1} to 1386 cm^{-1} and the C–N vibration of the aromatic ring stretched from 767 cm^{-1} to 782 cm^{-1}, indicating that the central Eu^{3+} ion was chelated to the DPA ligand *via* coordination with the N atom of the pyridine ring and the O atom of the carboxylic acid group, respectively. The broad absorption peak of N–H at 3105 cm^{-1} is due to the lone pair protonation of the pyridine nitrogen in the FT-IR spectra of Eu-DPA. The characteristic peaks at 3495 cm^{-1}, 1629 cm^{-1}, and 1076 cm^{-1} represented the stretching vibrations of O–H/N–H, C═O asymmetric tensile vibration and C═O bending vibration, respectively.[25] In addition, the FT-IR spectra of CQDs also corresponded to the tensile vibration of N–H and the asymmetric tensile vibration of C═O. All of the results confirmed that the surface of Eu-DPA–CQDs was rich in –COOH, $–NH_2$, –CO, and –NH– groups, which made the hybrid material more hydrophilic in an aqueous solution, thereby facilitating a better coordination of CQDs with Eu-DPA in aqueous solution detection applications. Fig. S2 (ESI†) shows the TEM image of CQDs; the average particle size is below 6 nm, which shows that the CQDs have a uniform dispersion.[26]

XPS patterns also confirmed the surface composition and chemical environment of Eu-DPA–CQDs. As shown in Fig. 2(A), the four peaks at 1134.70, 530.20, 398.70, and 283.30 eV correspond to Eu3d, O1s, N1s, and C1s. Compared with the N1s spectrum of CQDs (Fig. 3C), it can be clearly seen that the spectrum of N1s of Eu-DPA–CQDs (Fig. 2B) contained a new peak of pyridine N (399.15 eV), indicating the existence of DPA with the nitrogenous functional groups. In addition, the spectrum of O1s exhibited two fitted peaks at 532.80 and 531.46 eV, corresponding to the C–OH and C═O groups. All of the results of the XPS spectra are consistent with those of the FT-IR analysis, suggesting that the C═N and $–NH_2$ active groups on the surface of CQDs can provide potential coordination sites for chelating the central Eu^{3+}.

3.2 Photophysical properties of Eu-DPA–CQDs

The optical properties of Eu-DPA–CQDs were characterized *via* FL spectroscopy and UV-Vis spectroscopy. The excitation spectrum of Eu-DPA–CQDs measured at the characteristic

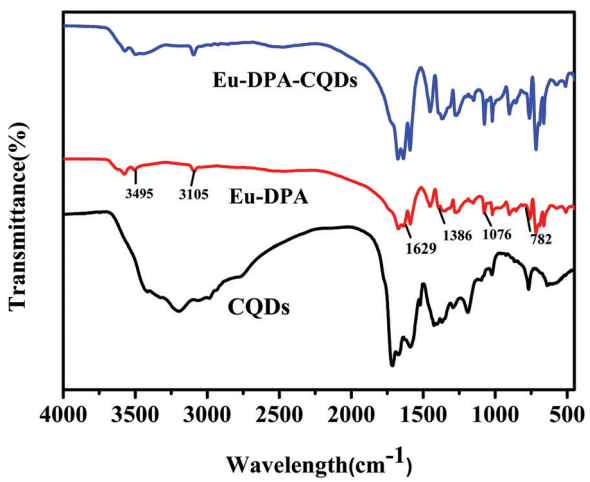

Fig. 1 FT-IR spectra of CQDs (black line), Eu-DPA (red line) and Eu-DPA–CQDs (blue line).

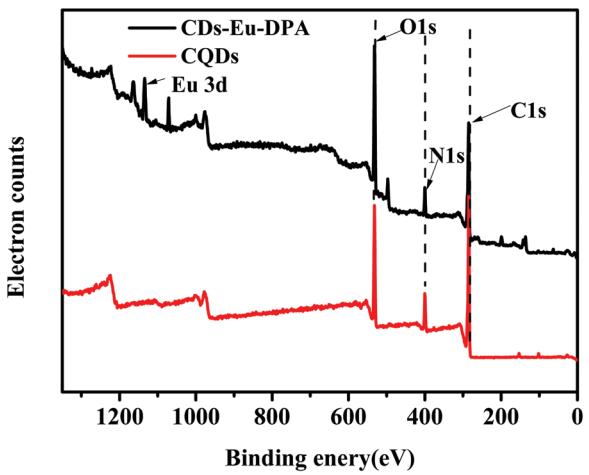

Fig. 2 XPS spectra of CQDs and Eu-DPA–CQDs.

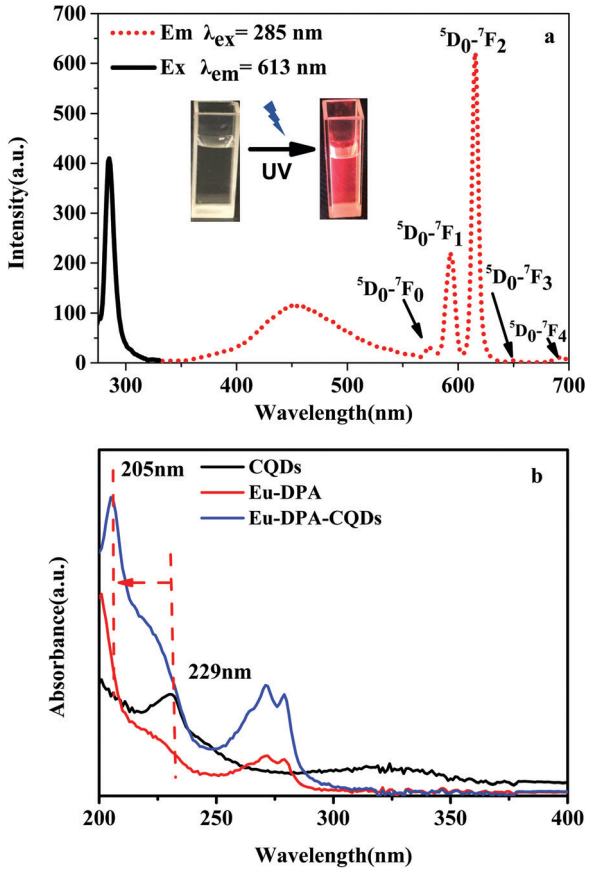

Fig. 3 (a) The excitation (black dotted line) and the emission (red dotted line) spectra of the Eu-DPA–CQDs; inset shows the corresponding photographs under a UV-light irradiation. (b) The UV-Vis spectra of CQDs (black line), Eu-DPA (red line), and Eu-DPA–CQDs (blue line).

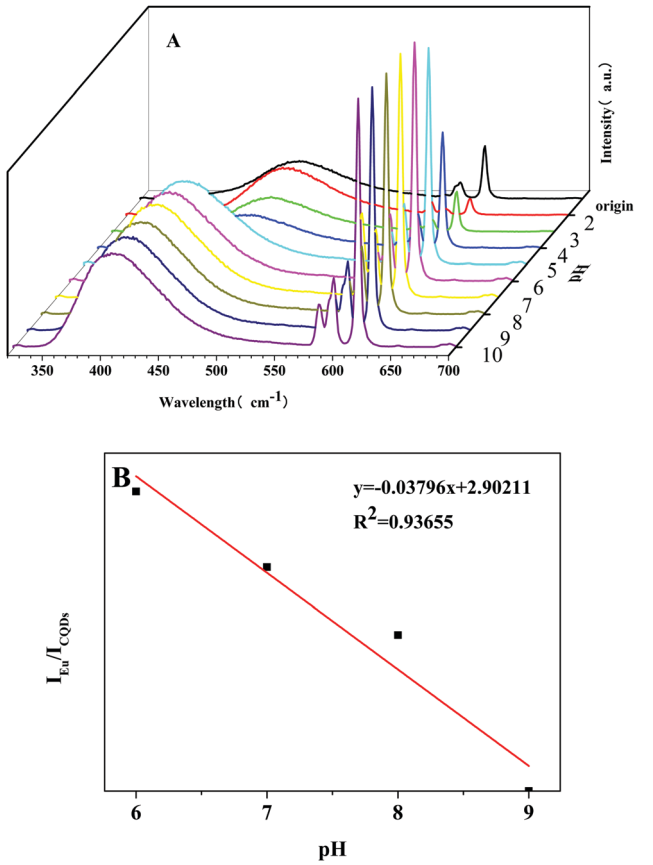

Fig. 4 (A) The relative fluorescence intensity of Eu-DPA–CQDs at different pHs. (B) The plot of the fluorescence intensity ratio (I_{Eu}/I_{CQDs}) *vs.* pH (6–9) in the linear fitting region.

emission of Eu^{3+} (λ_{em} = 613 nm), exhibited a sharp band with a maximum excitation peak at 285 nm. In the spectrum of Eu-DPA–CQDs, the characteristic emission bands of the central Eu^{3+} ions are evident as five peaks at 579, 590, 613, 653 and 701 nm, respectively, when excited at 285 nm, which are ascribed to the $^5D_0 \rightarrow {}^7F_J$ (J = 0–4) transitions (Fig. 3a). Moreover, a bright red emission can also be clearly observed under a UV lamp due to the transition from $^5D_0 \rightarrow {}^7F_J$ (inset of Fig. 3a). The emission wavelength at 613 nm is the strongest, indicating that the lattice occupied by Eu^{3+} ions had no inversion center and the crystal field symmetry was very low.[27,28] It is noteworthy to mention that there is a broad emission at 450 nm, which is caused by the functionalized surface of CQDs. The UV-Vis absorption spectra of CQDs, Eu-DPA and Eu-DPA–CQDs are shown in Fig. 3b. The obtained Eu-DPA–CQDs displayed two absorption peaks at 272 nm and 279 nm, which are attributed to the π–π* and n–π* transitions, respectively. The UV absorption peaks of CQDs at 229 nm are attributed to the π → π* transitions on the aromatic rings and the n → π* transitions of C=O on the CQD surface.[29,30] Compared to the absorption spectrum of CQDs, a blue-shift (205 nm → 224 nm) could be evidently observed in the spectrum of Eu-DPA–CQDs (Fig. 3b), suggesting the interaction between Eu-DPA and CQDs. The above results indicated that the successful synthesis of multi-emission fluorescence sensors has laid a foundation for the further construction of ratiometric fluorescence sensors. Therefore, optimal emission wavelengths are obtained with an appropriate excitation wavelength at 285 nm.

In addition, the photostability of Eu-DPA–CQDs was investigated under different pH values. By adjusting the pH of the solution, the fluorescence responses of Eu-DPA–CQD aqueous solution were measured (Fig. 4A). It can be observed that the fluorescence intensities of Eu^{3+} ions first gradually increased and then remained relatively stable in the pH range of 2–10. In particular, the emission peak is very strong and stable due to the antenna effect enhancement and the promotion of the photosensitization of Eu^{3+} ions under the alkaline conditions. Simultaneously, we also found about 60 nm blue-shift of the CQD emission peak with an increase in pH, which can be attributed to the surface plasmon resonance and quantum confinement effect, which resulted in the π* energy increment of the whole system.[31] After the coordination of C–N and Eu^{3+} ions, the charge transfer on the surface of CQDs also promoted the energy transfer between Eu^{3+} ions and DPA, which further confirmed the coordination formation between Eu^{3+} and CQDs. It is worth noting that it exhibits the strongest fluorescence at a pH of 6. Fig. 4B displays the good linear relationship of

I_{Eu}/I_{CQDs} in the pH range of 6–9. The calibration equation was $I_{Eu}/I_{CQDs} = -0.03796x + 2.90211$, and the determination coefficient (R^2) was 0.93655. According to the research by Marunaka *et al.*[32] under normal conditions, the pH of the human blood was between 7.35 and 7.45, and the most appropriate pH for the immune cells is also between 7.35 and 7.45. Similarly, the pH of the human skin is also in this range. In addition, when the pH value of the human body is lower than 7.3, the human body is in a sub-health state, which would cause a series of problems, such as body discomfort, lack of energy, and lack of physical strength. Similarly, when the body pH exceeds 7.45, it becomes alkaline and can be harmful. Therefore, Eu-DPA–CQDs with higher sensitivities can be used as ideal test probes to make further exploration in biology and successfully verify the potential of these probes in sensing pH.

3.3 Sensing and selectivity of metal ion detection

The potential application of Eu-DPA–CQDs for detecting metal ions had been examined. Eu-DPA–CQDs were immersed in an aqueous solution of 1 mmol L^{-1} MCl_x (M = Zn^{2+}, Mn^{2+}, Ni^{2+}, Cd^{2+}, Co^{2+}, Cu^{2+}, Fe^{2+}, and Fe^{3+}). The fluorescence behaviors are compared, as shown in Fig. 5A. The results revealed that the different metal ions displayed clearly different responses on the luminescence of the central Eu^{3+} ions. The presence of Cu^{2+} ions made Eu-DPA–CQDs to be completely quenched. This indicated that the quenching phenomenon might be due to the competitive interaction between Cu^{2+} and Eu^{3+} ions in Eu-DPA–CQDs. To further investigate the selectivity of the senor, the anti-interference ability to the co-existing ions was evaluated (Fig. 5B). It can be clearly seen that no significant difference in I_{Eu}/I_{CQDs} was observed in the presence or absence of these interfering metal ions. These results indicated the selectivity and anti-interference ability of the Eu-DPA–CQD ratio fluorescence sensor towards Cu^{2+} ions, further confirming its practical application in the detection of Cu^{2+} ions in our day life. Furthermore, in the presence of different concentrations of Cu^{2+} ions, we measured and recorded the fluorescence response of Eu-DPA–CQDs. As shown in Fig. 6, as the Cu^{2+} ion concentration increases (0–500 μM L^{-1}), the ratio of I_{Eu}/I_{CQDs} gradually increases, and there is a good linear relationship between the ratio of I_{Eu}/I_{CQDs} and the Cu^{2+} ion concentration (the correlation coefficient is $R^2 = 0.98026$), which can be calculated as an equation, $I_{Eu}/I_{CQDs} = -0.03973X + 5.26284$ (X is the concentration of Cu^{2+} ions, μM L^{-1}). According to the above equation and the standard of IUPAC 3σ(LOD = $3\sigma/k$),

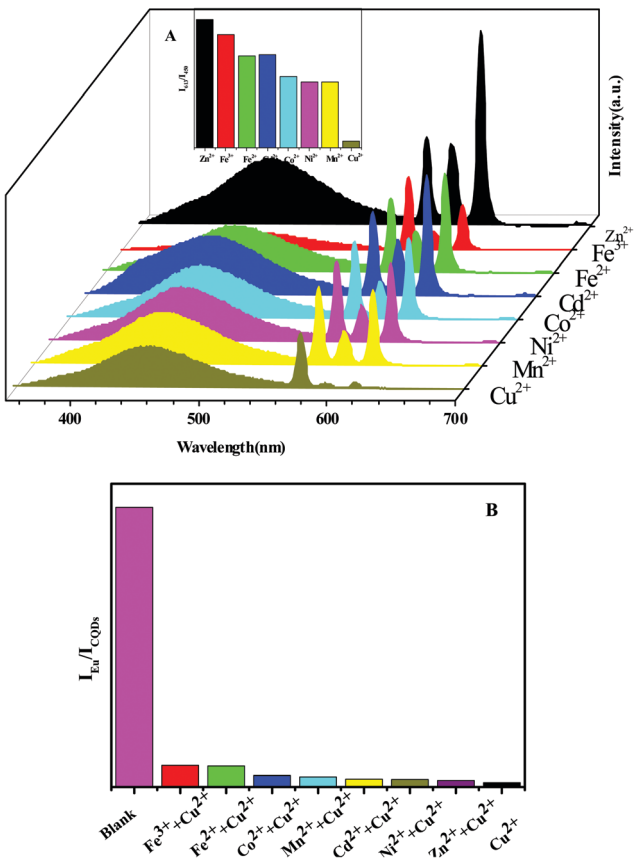

Fig. 5 (A) The emission spectra and the relative intensities of I_{613}/I_{450} for Eu-DPA–CQDs dispersed in different metal ion (10^{-3} mol L^{-1}) aqueous solutions. (B) I_{Eu}/I_{CQDs} of 500 μM Cu^{2+} ions and various co-existing metal ions.

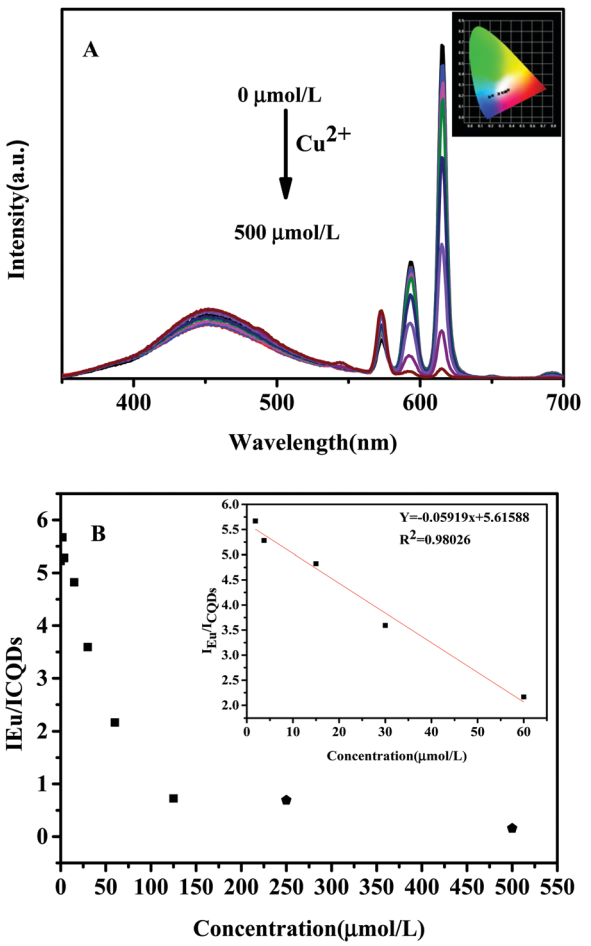

Fig. 6 The emission spectra of the Eu-DPA–CQDs immersed in aqueous solutions of Cu^{2+} ions at different concentrations (λ_{ex} = 285 nm).

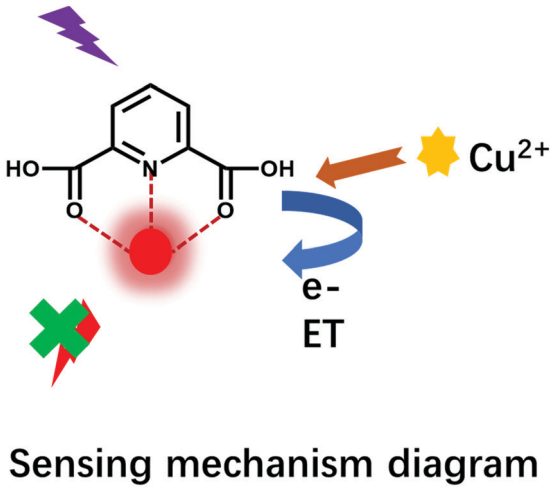

Fig. 7 The sensing mechanism of the fluorescence quenching of the Cu^{2+} ions.

the LOD is calculated to be 6 nM. Table S1 (ESI†) provides the previous report about the Cu^{2+} ion sensor based on CQDs. The results proved that the Eu-DPA–CQD hybrid material can be used as a right fluorescent nanosensor with excellent selective detection and sensitivity towards Cu^{2+} ions in an aqueous environment.

3.4 Sensing detection mechanisms

To explain the possible sensing mechanism of Eu-DPA–CQDs towards Cu^{2+} ions, their luminescence quenching effects were analyzed further. The performance of the Cu^{2+} ions on the luminescence intensity of the Eu-DPA–CQDs sensor is shown in Fig. 7. The possible sensing mechanism of the fluorescence quenching of the Eu-DPA–CQDs by the Cu^{2+} ions was speculated as follows: The FL emission peak of Eu was quenched significantly at 613 nm, and the quenching rate was ~88.60% (Effq (%) = $(I_0 - I)/I_0$, where I and I_0 represented the FL intensity of Eu-DPA–CQDs at 613 nm in the presence and absence of Cu^{2+} ions, respectively), while the FL of CQDs at 454 nm demonstrated almost no change as the concentration of Cu^{2+} ions increased. The electronic structure of CQDs and the distribution of excitons can be affected by the chemical bond. This process allowed the charge or energy transfer process to promote the non-radiative recombination of excitons and resulted in the energy transfer of the excited electrons from the ligand DPA to the half-filled 3d orbitals of Cu^{2+} ions, which led to an evident fluorescence quenching. In addition, there is a competitive absorption relationship between the Cu^{2+} ions and the unsaturated lanthanide complex, which hindered the energy transmission efficiency between the ligand and the lanthanide, and the antenna effect is weakened, resulting in the quenching of Ln^{3+} fluorescence.

4. Conclusion

In summary, a novel lanthanide functionalized CQD ratiometric fluorescence hybrid probe, which was coordinated by CQDs and $Eu(DPA)_3$ at room temperature, was successfully assembled through the surface modification of CQDs and Eu^{3+} chelation. Furthermore, the as-prepared Eu-DPA–CQDs demonstrated the dual characteristic emission peaks of both CQDs and Eu^{3+} ions, which had also demonstrated an outstanding luminescence property and different responses to numerous mental cation ions in water solution. As a result, the fluoresce intensity of Eu^{3+} ions at 613 nm was remarkably quenched in the presence of Cu^{2+} ions, while that of CQDs at 450 nm was slightly changed. Moreover, the energy transfer efficiency (antenna effect) between the lanthanide Eu^{3+} ions and the DPA ligands was interfered by the addition of Cu^{2+} ions, and the Eu-DPA–CQD sensor could be used in the determination of Cu^{2+} ions with a high selectivity and anti-interference ability.

Conflicts of interest

There are no conflicts of interest to declare.

Acknowledgements

This work was financially supported by the National Natural Science Foundation of China (21101107 and 51173107), the State Key Laboratory of Pollution Control and Resource Reuse Foundation (no. PCRRF19017) and Shanghai Engineering Technology Research Center for High-Performance Medical Device Materials (20DZ2255500).

References

1 S. R. Lynch, *Nutr. Rev.*, 1997, **55**, 102–110.
2 L. M. Hyman and K. J. Franz, *Coord. Chem. Rev.*, 2012, **256**, 2333–2356.
3 P. Wu, Y. Li and X.-P. Yan, *Anal. Chem.*, 2009, **81**, 6252–6257.
4 Y. Ding, H. Zhu, X. Zhang, J. J. Zhu and C. Burda, *Chem. Commun.*, 2013, **49**, 7797–7799.
5 T. Nguyen Duc, R. El Zein, J. M. Raimundo, H. Dallaporta and A. M. Charrier, *J. Mater. Chem. B*, 2013, **1**, 443–446.
6 X. Ren, L. Liu, Y. Li, Q. Dai, M. Zhang and X. Jing, *J. Mater. Chem. B*, 2014, **2**, 5541–5549.
7 R. Atchudan, T. Edison, K. R. Aseer, S. Perumal, N. Karthik and Y. R. Lee, *Biosens. Bioelectron.*, 2018, **99**, 303–311.
8 F. Pan, X. Xiang and Y. Li, *Eng. Sci.*, 2018, **1**, 21–32.
9 J. Di, J. Xia, X. Chen, M. Ji, S. Yin, Q. Zhang and H. Li, *Carbon*, 2017, **114**, 601–607.
10 Z. Wang, H. Liao, H. Wu, B. Wang, H. Zhao and M. Tan, *Anal. Methods*, 2015, **7**, 8911–8917.
11 T. Liu, J. X. Dong, S. G. Liu, N. Li, S. M. Lin, Y. Z. Fan, J. L. Lei, H. Q. Luo and N. B. Li, *J. Hazard. Mater.*, 2017, **322**, 430–436.
12 R. Zhang and W. Chen, *Biosens. Bioelectron.*, 2014, **55**, 83–90.
13 L. Li, C. Wang, J. Luo, Q. Guo, K. Liu, K. Liu, W. Zhao and Y. Lin, *Talanta*, 2015, **144**, 1301–1307.

14 M. Amjadi, J. L. Manzoori, T. Hallaj and N. Azizi, *J. Lumin.*, 2017, **182**, 246–251.
15 Y. Dong, R. Wang, G. Li, C. Chen, Y. Chi and G. Chen, *Anal. Chem.*, 2012, **84**, 6220–6224.
16 P. Singhal, B. G. Vats, S. K. Jha and S. Neogy, *ACS Appl. Mater. Interfaces*, 2017, **9**, 20536–20544.
17 D. Pooja, S. Saini, A. Thakur, B. Kumar, S. Tyagi and M. K. Nayak, *J. Hazard. Mater.*, 2017, **328**, 117–126.
18 B. Li, S. Zhan, H. Wang, B. Hou and G. A. J. Amaratunga, *Adv. Mater. Technol.*, 2020, **5**, 2000372.
19 F. Yuan, Y.-K. Wang, G. Sharma, Y. Dong, X. Zheng, P. Li, A. Johnston, G. Bappi, J. Z. Fan, H. Kung, B. Chen, M. I. Saidaminov, K. Singh, O. Voznyy, O. M. Bakr, Z.-H. Lu and E. H. Sargent, *Nat. Photonics*, 2019, **14**, 171–176.
20 P. de Almeida Rodrigues, R. G. Ferrari, L. N. Dos Santos and C. A. Conte Junior, *J. Environ. Sci.*, 2019, **84**, 205–218.
21 J. C. Bunzli, *Chem. Rev.*, 2010, **110**, 2729–2755.
22 M. S. Tremblay, Q. Zhu, A. A. Marti, J. Dyer, M. Halim, S. Jockusch, N. J. Turro and D. Sames, *Org. Lett.*, 2006, **8**, 2723–2726.
23 Z. Liu, W. He and Z. Guo, *Chem. Soc. Rev.*, 2013, **42**, 1568–1600.
24 Y. Fujiwara, J. A. Dixon, R. A. Rodriguez, R. D. Baxter, D. D. Dixon, M. R. Collins, D. G. Blackmond and P. S. Baran, *J. Am. Chem. Soc.*, 2012, **134**, 1494–1497.
25 Y. Tang, L. Rao, Z. Li, H. Lu, C. Yan, S. Yu, X. Ding and B. Yu, *Sens. Actuators, B*, 2018, **258**, 637–647.
26 H. Qi, M. Teng, M. Liu, S. Liu, J. Li, H. Yu, C. Teng, Z. Huang, H. Liu, Q. Shao, A. Umar, T. Ding, Q. Gao and Z. Guo, *J. Colloid Interface Sci.*, 2019, **539**, 332–341.
27 Y.-Y. Liu, R. Decadt, T. Bogaerts, K. Hemelsoet, A. M. Kaczmarek, D. Poelman, M. Waroquier, V. Van Speybroeck, R. Van Deun and P. Van Der Voort, *J. Phys. Chem. C*, 2013, **117**, 11302–11310.
28 S. W. Thomas, 3rd, G. D. Joly and T. M. Swager, *Chem. Rev.*, 2007, **107**, 1339–1386.
29 K. Shi, Z. Yang, L. Dong and B. Yu, *Sens. Actuators, B*, 2018, **266**, 263–269.
30 H. Chen, Y. Xie, A. M. Kirillov, L. Liu, M. Yu, W. Liu and Y. Tang, *Chem. Commun.*, 2015, **51**, 5036–5039.
31 C. Sakdaronnarong, A. Sangjan, S. Boonsith, D. C. Kim and H. S. Shin, *Catalysts*, 2020, **10**, 320–329.
32 Y. Marunaka, *Int. J. Mol. Sci.*, 2018, **19**, 3244.